3D High-Quality Magnetic Resonance Image Restoration in Clinics Using Deep Learning

Hao Li *, Jianan Liu *

***Abstract*— Shortening acquisition time and reducing the motion artifacts are two of the most essential concerns in magnetic resonance imaging. As a promising solution, deep learning-based high-quality MR image restoration has been investigated to generate highly-resolved and motion artifact-free MR images from lower resolution images acquired with shortened acquisition time or motion artifact-corrupted images. However, numerous problems still exist to prevent deep learning approaches from becoming practical in the clinic environment. Specifically, most of the prior works focus solely on the network but ignore the impact of various down-sampling strategies on the acquisition time. Besides, the long inference time and high GPU consumption are also the bottlenecks to deploy most of the prior works in clinics. Furthermore, prior studies employ random movement in retrospective motion artifact generation, resulting in uncontrollable severity of motion artifact. More importantly, doctors are unsure whether the generated MR images are trustworthy, making diagnosis difficult. To overcome all these problems, we adopted a unified framework of 2D deep learning neural network for both 3D MRI super-resolution and motion artifact reduction, demonstrating such a framework can achieve better performance in 3D MRI restoration tasks compared to other state-of-the-art methods and remain the GPU consumption and inference time significantly low, thus easier to deploy. We also analyzed several down-sampling strategies based on the acceleration factor, including multiple combinations of in-plane and through-plane down-sampling, and developed a controllable and quantifiable motion artifact generation method. At last, the pixel-wise uncertainty was calculated and used to estimate the accuracy of the generated image, providing additional information for a reliable diagnosis.**

***Index Terms*— MRI, 3D Super Resolution, In-plane and Through-plane down-sampling Strategy, Motion Artifact Generation, 3D Motion-Artifact Reduction, Aleatoric and Epistemic Uncertainty, Deep Learning for Clinic.**

I. Introduction

MAGNETIC resonance imaging (MRI) is used in a wide range of medical applications to aid precise diagnosis. However, doctors are frequently confronted with the resolution-acquisition time trade-off in the clinical environment, due to the capacity of hardware and the cooperation of patients. The acquisition of high-resolution (HR) magnetic resonance image consumes more scan time, and the patients cannot remain still for such a long period, resulting in a high probability of motion artifact. On the other hand, shortened acquisition time is more applicable for patients, whereas images with sufficient resolution can hardly be obtained. Therefore, with the capability to recover the resolution loss of HR images from low-resolution (LR) images and reduce the motion artifact, the deep learning-based super-resolution (SR) and motion artifact reduction (MAR) technique is a promising approach.

Super-resolution image reconstruction, as one of the major fields of computer vision, was deeply influenced by deep learning technology. In such a data-driven approach, a great amount of image pairs consisting of LR and corresponding HR images are collected as training data, and the deep neural network is trained to extract pixel-wise features and generate the SR image. Dong et al. [1] [2] first used this end-to-end learning-based method with a 2D convolutional neural network (CNN). Though larger neural network results in improved overall performance [3], training such a deep CNN has been demonstrated to be challenging [4]. Recently, Zhang et al. [6] proposed a network with channel attention and residual in residual structure with further enhanced performance in SR reconstruction.

Single image super-resolution (SISR) has been adopted into medical image sectors following the rapid advancement in natural images [8]–[10]. The majority of previous studies applied the 2D network structures to medical images slice by slice [9] [11]. However, medical images, like Computed Tomography (CT) and MRI, typically contain information about 3D anatomical structures. Processing each image slice independently may lead to a mismatch in the adjacent slices in the reconstructed images. As a result, 3D networks are desired to solve this problem due to their capacity of extracting 3D structural information. According to recent studies, 3D CNNs outperform 2D CNNs by a wide margin in MRI SR [12]–[14]. However, because of the extra dimension of 3D networks, the demand for a huge amount of GPU resources, as well as longer inference time prevent 3D neural networks to be deployed easily in real clinics. Although Chen et al. [12] [13] have demonstrated fast 3D networks, the margin between the GPU consumption and the inference time of 2D and 3D networks is still huge.

Regarding the synthetic LR image generation, the methods transferred from computer vision tasks, such as bicubic and Gaussian blurring [14] [15], don't consider the scheme of MR image acquisition, leading to the gap in degradation between synthetic training data and real MR images, thus

* Hao Li and Jianan Liu contribute equally to the work and are co-first authors. Order is alphabetical.

Jianan Liu is with Vitalent Consulting, Gothenburg, Sweden, and Silo AI, Stockholm, Sweden.

Hao Li is with the Department of Neuroradiology, University Hospital Heidelberg, Heidelberg, Germany.

degrade the performance of image restoration in the real clinics. The k-space truncation is recently recognized as the way of mimicking real LR image acquisition in MRI [17]. Besides, multiple down-sampling strategies have been employed in previous research. In the studies of 2D networks, $2 \times 2 \times 1$ (frequency-encoding (FE)$\times$phase-encoding (PE)$\times$slice-encoding (SL)) and $4 \times 4 \times 1$, as $\times 2$ and $\times 4$ in-plane down-sampling, were commonly used [15] [17]. And for 3D networks, HR images were down-sampled with scale factors of $1 \times 1 \times 2$, $1 \times 2 \times 2$ or $2 \times 2 \times 2$ [12] [18]–[20]. These down-sampling strategies lead to various acceleration factors in acquisition time and different difficulties for SR reconstruction. Therefore, for down-sampling strategies with the same acceleration factor, a properly selected down-sampling strategy with lower difficulty in SR reconstruction can result in improved performance and more accurate diagnosis. However, the down-sampling strategies were not analyzed in previous studies.

Furthermore, patient movement is inevitable during MRI measurements, resulting in motion artifacts (MA) that degrade the image quality. Deep learning algorithms can also reduce the MA and restore the MA-free images [21] [22],Most of the previous studies used 2D UNet-based networks to reduce the MA [23] [24], whereas 3D networks may improve the performance of motion artifact reduction while facing the same GPU consumption issue. Besides, previous studies normally used random movement to retrospectively generate MA [25]–[27], making the severity of the MA uncontrollable and irreproducible.

At last, doctors are frequently concerned about the accuracy of restored high-quality images. Tanno et al. [28] and Qin et al. [29] employed a method to predict aleatoric uncertainty for reconstructed image [31] as auxiliary information to assist doctors. However, such a method cannot distinguish whether the uncertainty is caused by the noise in the training data or caused by the error from the deep neural network due to out of distribution (OOD) data, i.e., the distribution of training data is not identical to the distribution of test data which is commonly seen in the real clinical environment. The latter is the actual uncertainty which reflects the quality of the restored MR image. On the other hand, the ground-truth (GT) images are available during the training and evaluation of the deep neural network, and the performances of the algorithms are evaluated by calculating the difference or similarity between the output images and the GT using some specific metrics. However, when we apply the deep-learning techniques in clinical settings, GT is no longer available, this Scenario necessitates the use of quantitative methods to estimate the accuracy of restored MR images at both pixel level and overall level to assist the medical doctors to make a trustworthy diagnostic.

Therefore, with considering the applications of deep learning based MR image restoration, we propose the following methods as contributions in this manuscript:

- 1). We propose a universal convolutional neural network modified from the 2D residual channel attention network [6] [7] with multiple slices input, for multi-tasks in high quality MR image restoration including 3D MRI super resolution and motion artifact reduction. Our model achieved state-of-the-art performance with minimized demands on computation resource and inference time.
- 2). We investigated a variety of down-sampling strategies, including in-plane down-sampling, through-plane down-sampling, and their combination with different scale factors. These down-sampling strategies were grouped based on the acquisition time reduction ratio. The super-resolution reconstruction performance was evaluated and compared in each down-sampling strategy group. The results illustrate the difficulties of super-resolution reconstruction with different down-sampling strategies and provide a guideline for selecting appropriate low-resolution image acquisition strategies.
- 3). We propose a method for retrospectively generating reproducible and quantifiable motion artifacts. With our method, motion artifacts were generated by mimicking the real motion artifact with a predefined motion pattern and controllable severity.
- 4). We developed a method for estimating the pixel-wise uncertainty quantification of generated SR images. The pixel-wise uncertainty was acquired concurrently with the restored images using the same deep neural network guided by an additional loss component in our method. The correlation between the uncertainty and SSIM / PSNR was further investigated and quantified in out study, providing more trustworthy advice in the diagnosis even when the ground truths are not available.

II. Methods and Experiments

A. Proposed MR image restoration network

The high-quality image restoration task entails creating a restoration system function $h(\bullet)$, which takes low quality (LQ) images (e.g., low-resolution images, or images with motion artifacts, etc.) and outputs the corresponding reconstructed images (e.g., SR or MA-free images) with high quality (HQ). This restoration function is considered as the inverse of the degradation function $f(\bullet)$, which represents the degradation from the HQ images to the LQ images:

$$HQ = h(LQ) \tag{1}$$

$$HQ = h(LQ) = f^{-1}(LQ) \tag{2}$$

Prior studies indicate that such a task is an ill-posed inverse problem, with no analytical solution to the inverse of $f(\bullet)$. Computer vision studies have revealed the great potential of CNN-based networks to fit the inverse of $f(\bullet)$.

B. Proposed High Quality MR image Restoration Network

Our network of thin slab RCAN (TS-RCAN) was developed based on the 2D Residual Channel Attention Network (RCAN) [6] [7], which has been proposed in the field of generic computer vision to generate the SR image from the LR image. Fig.1 depicts the basic pipeline of our model for high-quality MRI reconstruction. A dedicated module called

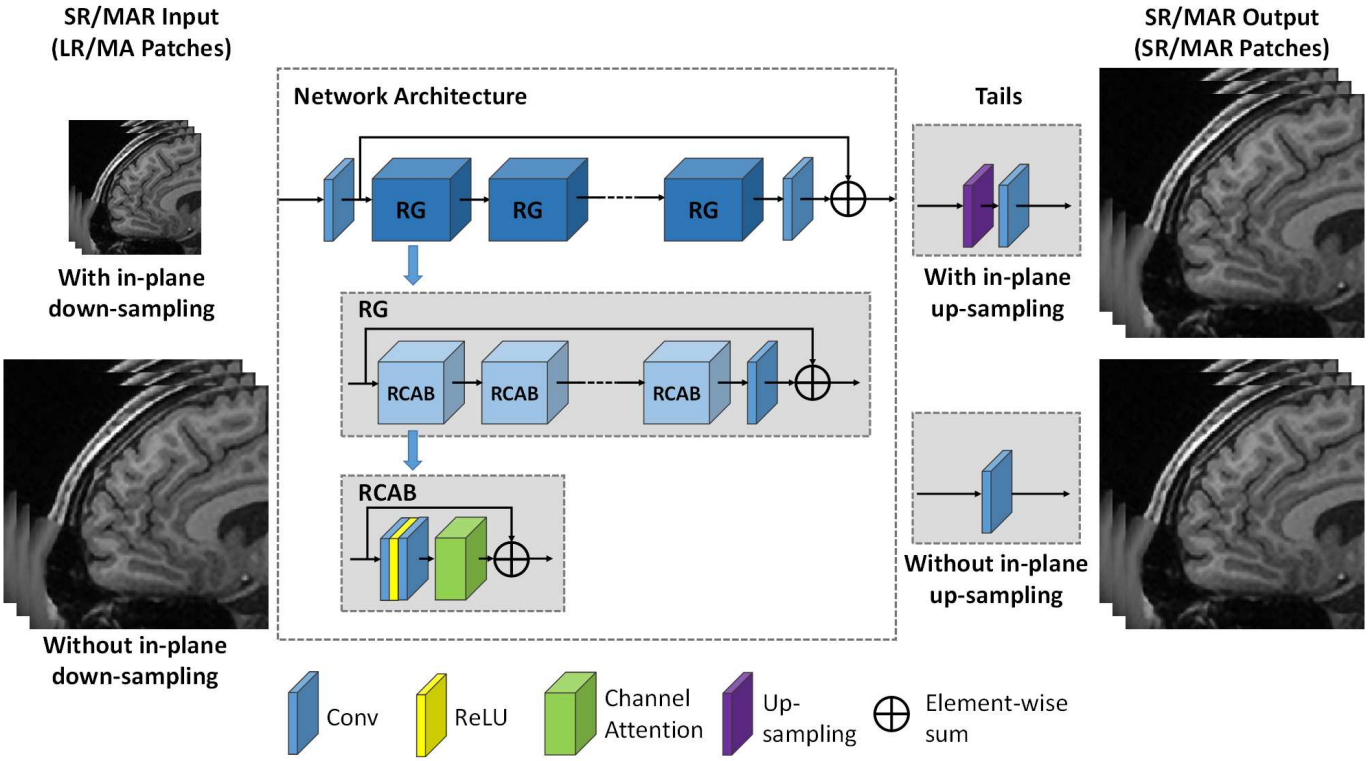

Fig. 1: The pipeline of RCAN based MRI SR and MAR network

channel attention (CA) layer is embedded into every residual block in the majority of our model to form a residual channel attention block (RCAB) [5]. A residual group (RG) is formed by several RCABs and a long skip connection, and the same pattern has also been extended to form a residual in residual (RIR) module, which also includes several RGs and a long skip connection. The attention weights for different channels that carry the statistics of semantic information of the MR image feature maps will be learned and used to guide the network focusing on restoration of the more important semantic information. Meanwhile, the skip connection in RCAB, RG, and RIR could provide the possibility of training the network model at a quick pace, especially if the network focuses on learning high frequency information by directly bypassing low frequency information. Back propagation is used to adjust all of the network's weights, which is driven by the minimization of the primary and refinement loss functions, which represent differences between predicted HQ MR images and ground truth images. When the LR images in the super resolution task are downscaled, the upsampling module performs the upscaling operation on the learned feature maps, resulting in the same size of the SR and HR images.

In the MRI SR task, the HR images had a larger matrix size compared to the generated LR images along the down-sampled directions. We constructed the RCAN model with N RGs, M RCABs per RG, and an up-sampling module if an in-plane upscaling image is needed. The 2D LR images with a single channel or the 3D LR images with the third dimension placed on the channels were processed to generate corresponding 2D/3D SR images. In the motion artifact reduction task, the MA corrupted images have the same size as the MA reduced (MAR) images, so the upsampling module was removed.

In our experiment, we used the 2D RCAN-based network to process both single-slice 2D (as in 2D mode) and thin-slab 3D (as in 3D mode) MR image patches. The 2D network is intrinsically capable of processing 3D datasets because of its channel dimension. Therefore, the network was applied in a multi-channel input and multi-channel output mode, with the third dimension of the 3D image patch placed on the channel dimension. We assume the first convolutional layer of the network has the number of input channels as $M (M \leq 5)$ and the number of output channels as N, and the size of the input image patches $M \times H \times W$. Therefore, the convolution kernel size of the first layer is $N \times M \times H \times W$, which works equally to the convolution with a 3D convolution kernel, whose size is $N \times 1 \times M \times H \times W$ with non-padding. In this step, features of multiple input slices were extracted and compressed into a single channel feature map for N times with different filters. Afterwards, these extracted features are learnt to reconstruct the high quality images in the hidden layers. At the last convolutional layer of the network, the number of the output channels equals the expected slice number of the target patch. The only difference between our 2D network and conventional 3D networks in this scenario is the smaller number of slices in each patch, which prevents through-plane features from being extracted over a larger slice range. Our experiments revealed that the features extracted from a thin-slab volume were sufficient for reconstructing high quality multi-slice images, and our model outperformed 3D networks and demand minimal computation resources.

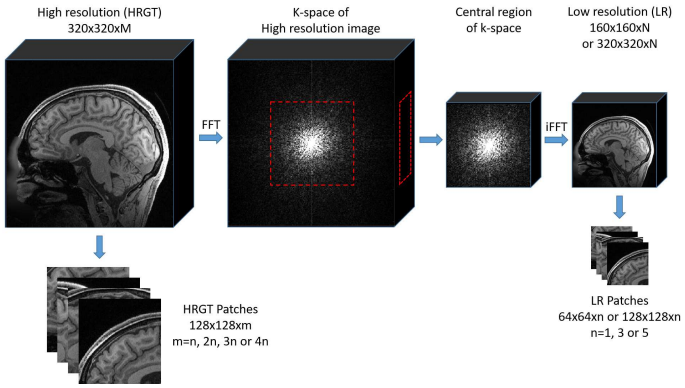

Fig. 2: Generation of 3D LR MR images with scale factor of 2 in three directions and patch cropping

In addition, we used a simple and effective approach of self-ensemble in our experiments to further improve the performance instead of the network-based [] and the data-based ensemble methods [], as the traditional ensemble methods require more training time or operation complexity. The thin slab patches consisted of several slices, each of which appeared in different places in different patches and was processed by the network differently, resulting in multiple outputs for the same image slice. Our experiments revealed that the average of all the outputs for the same slice achieved higher values in all metrics than every output image of this slice. Our method didn't require any additional operations or training time.

C. Down-sampling Strategies for Super-resolution

A 3D K-space truncation was used in our study to generate LR images from HR images. The HR images were transformed to K-spaces using 3D Fast Fourier Transformation (FFT), and the K-spaces were truncated in three dimensions according to the scale factors and only the central region of the K-spaces were remained. Then the truncated K-spaces were transformed to LR images using 3D inverse FFT (iFFT). At last, the intensities of voxels for both HR and LR images were scaled to the range of 0 to 1. Fig.2 shows an example of 3D LR MR image generation.

The acquisition time of 3D MRI highly depends on phase-encoding steps in the PE and SL directions, thus only down-sampling in PE and SL directions shorten the acquisition time. However, in regular MRI measurements, the resolutions in the PE and FE directions always change simultaneously with the same scale factor to maintain the isotropic in-plane resolution, resulting in an unnecessary loss of K-space in the FE direction and greater difficulty in restoring the HR image. Meanwhile, the slice thickness is independent of the in-plane resolution and can be down-sampled with greater flexibility. More specifically, when a $\times 2$ acceleration is expected, there are two down-sampling options, which are $2\times2\times1$and $1\times1\times2$. With the $2 \times 2 \times 1$ down-sampling, 75% of the K-space is dropped, while with $1 \times 1 \times 2$ only 50% of the K-space is dropped.

However, the difficulty of restoring the HR image is not solely determined by the ratio of K-space truncation. The more low-frequency components of the K-space are dropped, the more difficult it is to restore the HR image. In this study, we investigated multiple down-sampling strategies and their SR reconstruction performances. Based on the regular MRI measurement process, we tested the SR reconstruction with the down-sampling factors of $2 \times 2 \times 1$ and $1 \times 1 \times 2$ for $\times 2$ acceleration, and $4 \times 4 \times 1$, $2 \times 2 \times 2$, and $1 \times 1 \times 4$ for $\times 4$ acceleration.

After down-sampling, the HR and LR images were cropped into patches of smaller sizes to save computation resources. The HR images was cropped into 128×128 patches with 32 voxels overlapped between neighboring patches to avoid artifacts on the edges of the patches. The LR images were cropped into 64×64 patches with 16 voxels overlapped for a scale factor of 2 and 32×32 patches with 8 voxels overlapped for a scale factor of 4. Each LR patch contains 1/3/5 neighboring slices from the LR image with $n-1$ slices overlapped between neighboring patches, and the number of slices for the HR patch is 1/3/5 times the scale factor in the SL direction. For other conventional 3D networks used for comparison, the LR images were interpolated to the same matrix size as the HR images, since 3D networks don't have an up-sampling module. Both the HR and LR images were cropped into $64 \times 64 \times 64$ patches with 32 voxels overlapped between neighbouring patches.

D. Motion Pattern and Motion Artifact Quantification

The method of splicing lines from multiple K-spaces was used to simulate the generation of real motion artifacts in MR images for the retrospective generation of motion artifacts. As shown in Fig.3A, a group of images was generated from the original image volume by rotating it in specific directions and to specific degrees. The original image and generated images were then transformed to K-space using FFT, and K-space segments of the original image were replaced with segments from the generated images' K-spaces, according to a predefined pattern. The images for the motion-artifact correction task were not cropped, so the axial sizes of the input MA and GT images were 320×256.

Regarding the motion patterns, we employed simplified and commonly-recognized patterns of motion in brain imaging, which were head rotation as the in-plane movement and nodding as the through-plane movement, and the severity was managed by the frequency of motion. The scheme of the motion pattern is depicted in Fig.3B. We used echo-group (EG) as a unit of the minimal time period in which a certain number of successive echoes were acquired (which can also be considered as the TR for sequences from the turbo-spin-echo family), and the duration of any action must be an integer multiple of EG. In terms of the type of movement, we used head rotations of 5 degrees to the left and to the right, with and without head nodding by 5 degrees. Therefore, the whole process of patient movement was set as below:

1) : at $t = 0$, the patient stayed in the original position and stayed for T_S;

2) : from $t = T_S$ to $t = T_S + 2EG$, the patient's head rotated to the left for 5 degrees;

3) : from $t = T_S + 2EG$ to $t = T_S + 7EG$, the patient's head stayed at the position of 5 degrees to the left;

4) : from $t = T_S + 7EG$ to $t = T_S + 9EG$, the patient's head rotated back to the starting position;

5) : from $t = T_S + 9EG$ to $t = 2T_S + 9EG$, the patient's head stayed in the starting position;

6) : from $t = 2T_S + 9EG$ to $t = 2T_S + 18EG$, the patient's head rotated to the right and returned to the starting position following the same process of step 2 to 4;

7) : from $t = 2T_S + 18EG$ to $t = 3T_S + 18EG$, the patient's head stayed in the starting position.

The process from steps 2 to 7 was repeated until the whole k-space was acquired, and head nodding was performed together with head rotating. The severity of motion artifacts was controlled by T_s and EG.

In our study, T_s was set to $9EG, 18EG, 36EG$ and $72EG$, leading to a corrupted k-space line ratio of $50\%, 33.3\%, 20\%$ and 11.1%. $1EG$ consists of 80 echos. A centric trajectory was selected to fill the k-space. The SSIMs and PSNRs of the images with different severities of motion artifacts follow a linear tendency as shown in Table III in the result section.

E. Uncertainty

In previous studies, the pixel-wise aleatoric uncertainty can be generated by incorporating Gaussian negative log likelihood (NLL) loss into neural network [30], and applied in MR super-resolution reconstruction [28] [29]. Such uncertainty only represents the uncertainty from data, which cannot be prevented, and it is not the main issue when applying the deep learning based MRI restoration in clinical practices. On the contrary, the inevitable OOD data issue (i.e., images acquired from different patients or from a different scanner may have diverse distributions in a real clinic environment due to image quality differences) can be represented by epistemic uncertainty [31]. In our study, both pixel-wise aleatoric uncertainty and epistemic uncertainty are estimated by using evidential regression [34]. Evidential deep learning formulates learning as an evidence acquisition process. Every training example adds support to a learned higher-order, evidential distribution. Sampling from this distribution yields instances of lower-order likelihood functions from which the data was drawn. Instead of placing priors on network weights, as is done in Bayesian neural networks, evidential approaches place priors directly over the likelihood function. By training a neural network to output the hyperparameters of the higher-order evidential distribution, a grounded representation of both epistemic and aleatoric uncertainty can then be learned without the need for sampling. Amini et al. proposed the method to estimate a posterior distribution $q(\mu, \sigma^2)$, and the approximation to the posterior distribution takes the form of the Gaussian conjugate prior, the Normal Inverse-Gamma (NIG) distribution $p(\mu, \sigma^2|\gamma, \upsilon, \alpha, \beta)$ [34]. Afterwards, the prediction and uncertainties can be calculated as:

$$Prediction : E[\mu] = \gamma \tag{3}$$

$$Aleatoric : E[\sigma 2] = \frac{\beta}{\alpha - 1} \tag{4}$$

$$Epistemic : Var[\mu] = \frac{\beta}{\upsilon(\alpha - 1)} \tag{5}$$

Furthermore, we investigated the relationships between epistemic uncertainty and the SSIM and PSNR metrics of the reconstructed images. Linear regression and exponential regression were performed to estimate the correlation of epistemic uncertainty to SSIM and PSNR for the test datasets, respectively. Then, the obtained regression curves can be used to estimate the SSIM and PSNR of the reconstructed images when ground truth is not available.

F. Loss Functions

In previous studies, different types of loss functions were used to train neural networks for specific feature refinements. In this study, pixel-wise Charbonnier loss [35] was used as a differentiable L1 loss to avoid a strong smoothing effect [36]:

$$L_{Char} = \frac{1}{N}\sum_{i=1}^{N}\sqrt{(HR_i - SR_i)^2 + \epsilon} \tag{6}$$

where ϵ is assigned as 10^{-4}.

Furthermore, in some of the most recent studies, SSIM loss is used to drive the network reconstructing the high quality images toward better structural similarity with the GT images. It is typically applied as 1 subtracted by the SSIM value measured between the reconstructed images and the GT images [37] [38]. In this study, we utilized the L1 loss of the square of the SSIM value to enhance the weight of SSIM loss:

$$L_{SSIM} = \frac{1}{N}\sum_{i=1}^{N} \mid 1 - SSIM(SR_i, HR_i)^2 \mid \tag{7}$$

The calculation of SSIM will be introduced in latter section.

In our study, we utilized the weighted sum of Charbonnier loss and SSIM loss for image restoration:

$$Loss = L_{Char} + \alpha_1 L_{SSIM} \tag{8}$$

where $\alpha_1 = 0.5$ in our study for the best performance.

Besides, the Normal-inverse-Gamma loss [34] was employed when the uncertainty map was demanded:

$$L_{NIG} = L_{NLL} + \lambda L_{Reg} \tag{9}$$

where

$$\begin{aligned} L_{NLL} = &\frac{1}{2}log(\frac{\pi}{\upsilon}) - \alpha log(\Omega) \\ &+(\alpha + \frac{1}{2})log((y-\gamma)^2\upsilon + \Omega) \\ &+log(\frac{\Gamma(\alpha)}{\Gamma(\alpha + \frac{1}{2})}) \end{aligned} \tag{10}$$

$$\Omega = 2\beta(1 + \upsilon) \tag{11}$$

$$L_{Reg} = \mid y - \gamma \mid (2\upsilon + \alpha) \tag{12}$$

α, β, γ and υ are the outputs of the network. y is the ground truth.

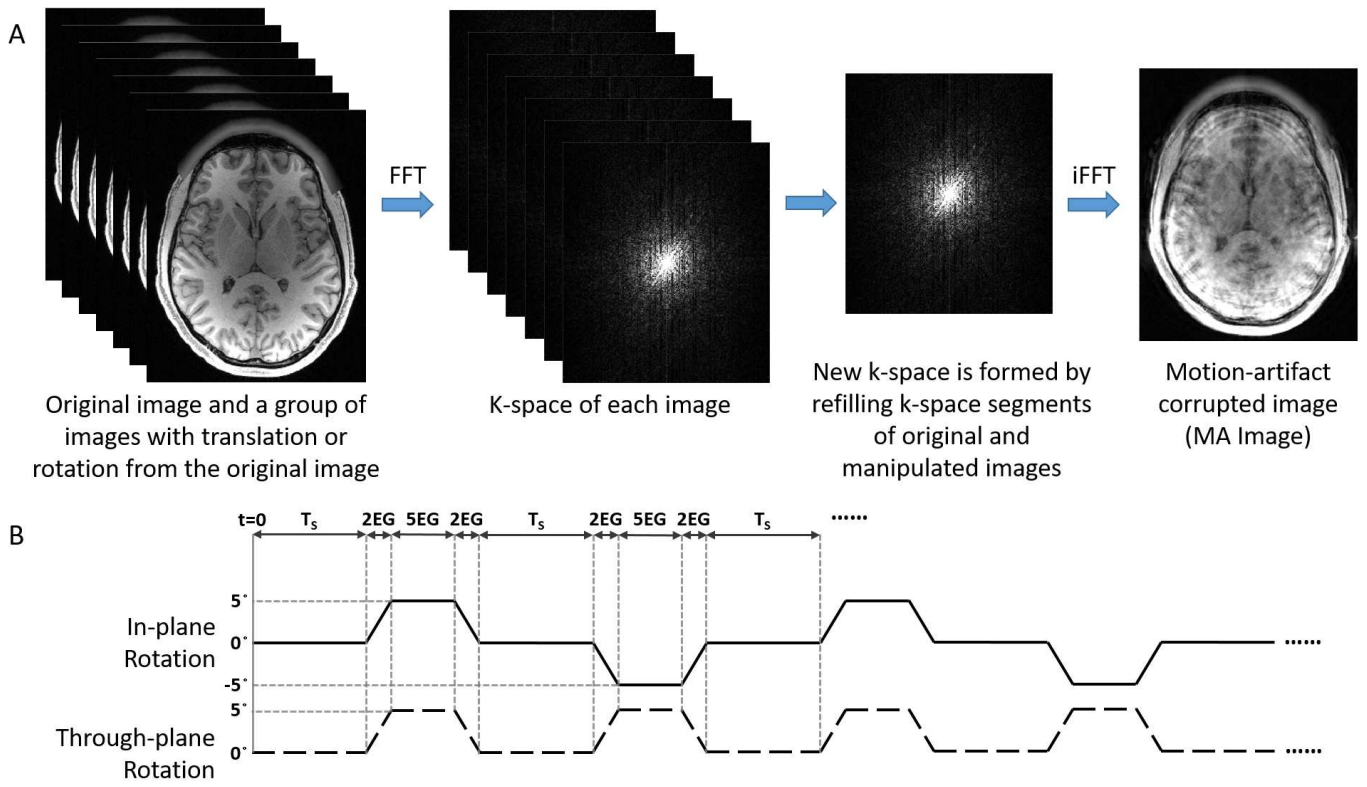

Fig. 3: A: Image-based generation of motion-artifact in MR images; B: Scheme of motion pattern employed in our study.

To summarize, we utilized the weighted sum of Charbonnier loss and SSIM loss for image restoration, and NIG loss when evidential regression was employed:

$$Loss = L_{Char} + \alpha_1 L_{SSIM} + \alpha_2 L_{NIG} \tag{13}$$

where 0.5 and 1 were selected as the value of α_1 and α_2 in our study for the best performance.

G. Datasets

In this study, we used the T1w images from the Human Connectome Project (HCP) dataset (35), consisting of multi-contrast images from 1113 patients. The T1w images were acquired in the sagittal direction with 3D MPRAGE on the Siemens 3T PRISMA platform. The matrix size was $320 \times 320 \times 256$, with an isotropic resolution of 0.7 mm. In our experiments, we randomly selected 80/10/10 patients from the HCP patient cohort for training/validation/test groups. The training datasets were used to train the neural networks, the validation datasets to monitor the neural networks' performance during training, and the test datasets to evaluate the neural networks after training. There were no shared datasets among the three groups. In addition, to verify the quantified correlation between uncertainty and SSIM/PSNR, we used another 40 patients which were isolated from the previously mentioned training/validation/test groups.

H. Implementation Details

In terms of RCAN implementation, for an SR factor of 2, an RG number of 5 was chosen, with 5 RCABs in each RG. The convolution layers in shallow feature extraction and the RIR structure had 64 filters, except that for channel downscaling. We connected two stages of the RCAN network sequentially for progressive-upsampling with an SR factor of 4. Each stage consisted of 3 RGs with 3 RCABs and one upsampling module upscaling the LR images by a factor of 2 at the end of each stage.

The networks were trained on a workstation equipped with two Nvidia Quadro GV100 graphic cards. For all deep learning experiments, we used Pytorch 1.7 as the back end. In each training batch, eight LR patches were randomly extracted as inputs. We trained our model for 50 epochs using the ADAM optimizer with $\beta_1 = 0.9$, $\beta_2 = 0.999$, and $\epsilon = 10^{-8}$, and a Cosine-decay learning rate was applied starting from 10^{-4} and ending at 10^{-8}. We employed peak signal-to-noise ratio (PSNR) and structure similarity index (SSIM) [37] to evaluate the quality of reconstructed images. Mann-Whitney U tests were performed to detect statistical difference among the results of different methods. All numerical analysis and data preprocessing were performed using MATLAB.

III. Results

A. Super-Resolution with Different Down-sampling Strategies

In this section, we will first assess our network's performance in 2D and 3D mode for SR image reconstruction from LR images generated by various down-sampling strategies, and then compare the difficulty of SR image reconstruction among these down-sampling strategies.

TABLE I: Comparison of SR performance with different down-sampling strategies (red represents the best and blue represents the second best)

Scale Factor	Acceleration Factor	# Input / Output Slices	# Params (M)	# Ops (GFlops)	Inference Time (s)	Axial SSIM / PSNR	Sagittal SSIM / PSNR	Coronal SSIM / PSNR
2 × 2 × 1	× 2	1 / 1	2.23	9.09	5.97	0.9630±0.0049 / 39.2521±1.3006	0.9625±0.0051 / 38.7468±1.3175	0.9628±0.0049 / 38.7723±1.4609
		3 / 3	2.23	9.12	5.93	0.9638±0.0049 / 39.3688±1.3533	0.9631±0.0051 / 38.8662±1.3566	0.9637±0.0049 / 38.9178±1.5334
		3 / 3 +	2.23	9.12	5.93	0.9644±0.0049 / 39.4410±1.3675	0.9634±0.0051 / 38.9355±1.3756	0.9643±0.0049 / 38.9922±1.5492
		5 / 5	2.24	9.14	5.86	0.9635±0.0049 / 39.2784±1.3172	0.9627±0.0051 / 38.7745±1.3252	0.9633±0.0049 / 38.8150±1.5070
		5 / 5 +	2.24	9.14	5.86	0.9642±0.0049 / 39.3681±1.3344	0.9631±0.0051 / 38.8605±1.3538	0.9641±0.0049 / 38.9079±1.5296
1 × 1 × 2	× 2	1 / 1	2.08	33.95	7.09	0.9548±0.0065 / 39.0363±1.4401	0.9558±0.0065 / 38.5996±1.1916	0.9547±0.0064 / 38.5506±1.4681
		3 / 3	2.09	33.99	7.16	0.9728±0.0043 / 41.2963±1.4897	0.9724±0.0044 / 40.7656±1.4778	0.9728±0.0043 / 40.9346 ±1.4831
		3 / 3 +	2.09	33.99	7.16	0.9732±0.0044 / 41.4162±1.5146	0.9725±0.0045 / 40.8979±1.5015	0.9731±0.0044 / 41.0656±1.5136
		5 / 5	2.09	34.05	6.87	0.9742±0.0041 / 41.4627±1.5223	0.9736±0.0042 / 40.9537±1.5115	0.9741±0.0041 / 41.1057±1.5279
		5 / 5 +	2.09	34.05	6.87	0.9747±0.0042 / 41.6226±1.5509	0.9739±0.0043 / 41.1143±1.5413	0.9747±0.0042 / 41.2747±1.5666
4 × 4 × 1	× 4	1 / 1	2.88	7.26	7.32	0.9303±0.0098 / 36.1333±1.5117	0.9272±0.0104 / 35.5164±1.4947	0.9301±0.0097 / 35.5728±1.5362
		3 / 3	2.88	7.38	7.17	0.9321±0.0091 / 36.2668±1.4271	0.9291±0.0098 / 35.6303±1.4204	0.9319±0.0090 / 35.6961±1.4784
		3 / 3 +	2.88	7.38	7.17	0.9335±0.0093 / 36.3601±1.4495	0.9300±0.0100 / 35.7243±1.4502	0.9332±0.0092 / 35.7916±1.5040
		5 / 5	2.88	7.40	7.54	0.9320±0.0098 / 36.2141±1.5265	0.9289±0.0103 / 35.4683±1.4140	0.9318±0.0096 / 35.6557±1.5058
		5 / 5 +	2.88	7.40	7.54	0.9347±0.0097 / 36.4120±1.5599	0.9301±0.0104 / 35.5939±1.4524	0.9345±0.0096 / 35.8613±1.5470
1 × 1 × 4	× 4	1 / 1	2.09	33.96	3.58	0.9045±0.0116 / 35.0832±1.2670	0.9148±0.0112 / 34.1939±1.2787	0.9047±0.0112 / 34.2843±1.1206
		3 / 3	2.09	34.05	3.57	0.9430±0.0096 / 37.7795±1.6113	0.9450±0.0090 / 36.9546±1.6488	0.9430±0.0096 / 37.2201±1.5327
		3 / 3 +	2.09	34.05	3.57	0.9433±0.0099 / 37.8987±1.6554	0.9449±0.0095 / 37.0753±1.7094	0.9433±0.0098 / 37.3525±1.5850
		5 / 5	2.10	34.15	3.38	0.9443±0.0091 / 37.8376±1.5973	0.9458±0.0087 / 37.0159±1.5824	0.9442±0.0090 / 37.3085±1.4690
		5 / 5 +	2.10	34.15	3.38	0.9451±0.0094 / 38.0384±1.6380	0.9463±0.0090 / 37.2224±1.6416	0.9451±0.0093 / 37.5271±1.5212
2 × 2 × 2	× 4	1 / 1	2.23	9.10	3.02	0.9331±0.0094 / 36.7213±1.2262	0.9356±0.0093 / 36.0732±1.1916	0.9331±0.0092 / 36.1325±1.1318
		3 / 3	2.24	9.15	2.98	0.9497±0.0079 / 38.1522±1.4506	0.9490±0.0080 / 37.5758±1.4242	0.9496±0.0078 / 37.6774±1.3922
		3 / 3 +	2.24	9.15	2.98	0.9507±0.0080 / 38.2623±1.4794	0.9494±0.0081 / 37.6909±1.4566	0.9506±0.0079 / 37.7964±1.4254
		5 / 5	2.24	9.19	2.97	0.9501±0.0078 / 38.1622±1.3875	0.9491±0.0079 / 37.5689±1.3742	0.9499±0.0078 / 37.6385±1.3457
		5 / 5 +	2.24	9.19	2.97	0.9514±0.0078 / 38.3026±1.4161	0.9498±0.0080 / 37.7166±1.4138	0.9513±0.0077 / 37.7945±1.3834

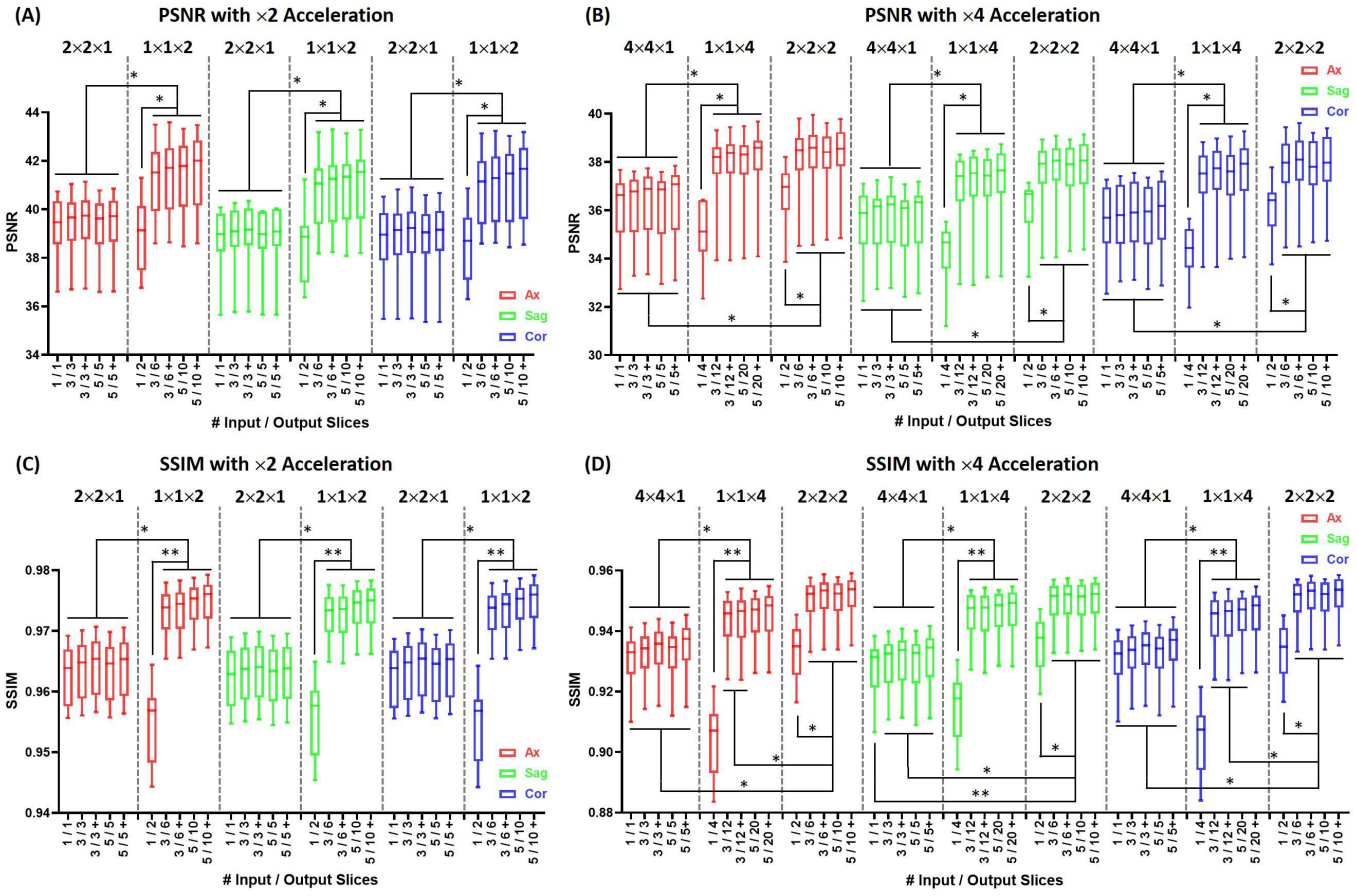

Fig. 4: Comparison of metrics of different scale factors. The scale factors are grouped based on the acceleration factor. (A)/(C): PSNR and SSIM of super-resolution images with ×2 acceleration ($2 \times 2 \times 1$ and $1 \times 1 \times 2$); (B)/(D): PSNR and SSIM of super-resolution images with ×4 acceleration ($4 \times 4 \times 1$, $1 \times 1 \times 4$ and $2 \times 2 \times 2$). '+' represents the SR reconstruction with self-ensemble. Mann-Whitney U tests compared whether the metrics of different down-sampling strategies were statistically different. Significant difference is indicated with $*p < 0.05$ and $**p < 0.0005$.

Table I shows the performance of SR reconstruction using our network for 2D and 3D SR. For all down-sampling strategies, 3D SR reconstruction outperformed 2D SR reconstruction. The mean SSIM and PSNR of SR images reconstructed with 3-slice input soared from single-slice input with significant difference observed. The mean SSIM and PSNR rose again with 5-slice input for the strategies with through-plane down-sampling, although significant difference was not detected. The mean SSIM and PSNR for the strategies with only in-plane down-sampling reached their peaks at 3-slice input and dropped slightly with 5-slice input. In addition, self-ensemble improved the performance of the 3D mode in the SR reconstruction for all down-sampling strategies.

Furthermore, the SR reconstruction performance is compared between different down-sampling strategies with the same acceleration factors. With $\times 2$ acceleration, the mean SSIM/PSNR values of $1 \times 1 \times 2$ down-sampling are over 0.01/2.2 dB higher than those of $2 \times 2 \times 1$ in three directions with significant difference observed (Fig. 4(A) and (C)). And with the $\times 4$ acceleration, the $2 \times 2 \times 2$ down-sampling has the highest mean values of SSIM/PSNR, which are over 0.003/0.3 dB higher than $1 \times 1 \times 4$ and 0.02/1.9 dB higher than $4 \times 4 \times 1$ in three directions with significant difference observed (Fig. 4(B) and (D)). The results reveal that it is easier to reconstruct accurate SR images from $1 \times 1 \times 2$ dowm-sampling for $\times 2$ acceleration and $2 \times 2 \times 2$ for $\times 4$ acceleration.

In addition to the difference in the metrics, the visual effect is compared in Fig.5. The 2D SR image shows errors in reconstructing small anatomical structures in the sagittal view, whereas the 3D SR image shows extensive accuracy in restoring small anatomical structures. Furthermore, there is a mismatch of neighboring slices in the axial view of the 2D SR image, but not in the 3D SR image (Fig. 5(A)). Fig.5(B) compares SR images from various down-sampling strategies with an acceleration factor of 4, highlighting the limitations of the $4 \times 4 \times 1$ and $1 \times 1 \times 4$ down-samplings for SR reconstruction. The reconstructed image of $4 \times 4 \times 1$ loses nearly all the small anatomical structures in the sagittal view and $4 \times 4 \times 1$ in the axial view, while the image reconstructed from $2 \times 2 \times 2$ is less blurry than the previous two with the majority of the small anatomical structures retained.

B. Super-Resolution Performance Compared with the State of the Art

We extended SRCNN and FSRCNN [2]to 3D mode, and implemented DCSRN [12], mDCSRN [13], ReCNN [16] and MINet [44] as the baseline for 3D SR. All models were trained with the same number of epochs and settings (i.e. learning rate decay and optimizer). With respect to quantitative similarity metrics, as shown in Table II and Fig. 6, our model with thin-slab SR highly outperformed all previous SISR models in 3D SR tasks, took less inference time and consumed less GPU resource than most of the previous models.

As shown in Table II and Fig. 6(A)-(D), for SR reconstruction of $2 \times 2 \times 1$ down-sampling, our network achieved 0.9631/38.8662 in mean SSIM/PSNR, which outperformed SRCNN, FSRCNN and DCSRN with significant differences. Although a significant difference was not observed, the mean SSIM/PSNR of our network were 0.004/1.7 dB and 0.001/0.2 dB higher than ReCNN and MINet, respectively. For SR reconstruction of $2 \times 2 \times 2$ down-sampling, our network outperformed SRCNN, FSRCNN and DCSRN with significant differences, and exceeded ReCNN by 0.002/1.2 dB and MINet by 0.000/0.2 dB in mean SSIM/PSNR.

As to the consumption of computation resources shown in Fig. 6(E)-(J) for $2 \times 2 \times 2$ SR reconstruction, the number of operations of our network was comparable to 3D SRCNN and 3D FSRCNN, and significantly lower than the other networks. The GPU consumption and the inference time were lower than all the other networks. Comparing to ReCNN and MINet, whose performances of SR reconstruction were closest to our network, our network consumed 60.4% and 63.5% lower VRAM than ReCNN and MINet, respectivele. The inference time of our network for processing the image of one patient was 11.2% and 15.7% of ReCNN and MINet.

Fig.7 illustrates the visual difference between the 3D SR of various networks with $2 \times 2 \times 2$ down-sampling. The reconstructed SR images of SRCNN, FSRCNN and DCSRN were highly blurry in both sagittal and axial view, while ReCNN, MINet and TS-RCAN showed comparable performance with enhanced accuracy in restoring small anatomical structures.

C. Motion Artifact Generation and Reduction

In previous studies, motion artifacts were typically generated by random movement and corrupting randomly selected k-space lines, resulting in non-reproducible motion artifact severity. Our motion artifact generation method employs predefined motion patterns with specific durations and repetitions at specific frequencies, resulting in controllable severity. As shown in Table III, the SSIMs and PSNRs of the motion artifact-corrupted images, which reveal the severity difference of motion artifacts, follow a consistent tendency as the T_s increases. When the T_s is doubled in the group with only in-plane rotation, the SSIM increases by 0.05 to 0.07 and the PSNR increases by 2.5 to 3.3 dB in all three directions. The SSIM and PSNR of the group with both in-plane and through-plane rotation exhibit the same pattern. Furthermore, the comparison between these two groups reveals that through-plane rotation results in additional decrements of 0.01 in SSIM and around 0.5 dB in PSNR.

Also demonstrated in Table III and Fig. 8, our network outperformed the UNet [23], which was widely used in previous studies, with considerable gains in SSIM and PSNR and significant difference detected. In 2D mode (1 slice input and output), our network highly outperformed the UNet with consistent improvements of 0.001 to 0.003 SSIM and 0.5 to 0.7 dB in PSNR for varying degrees of motion artifact severity. The performance of our network was further improved in 3D mode, with increments of 0.001 to 0.008 in SSIM and 0.3 to 0.6 dB in PSNR compared to 2D mode. Furthermore, the self-ensemble raised the SSIM and PSNR by another 0.001 and 0.1 dB, respectively.

The visual effects of motion artifact reduction are also compared, and our network shows significant improvement.

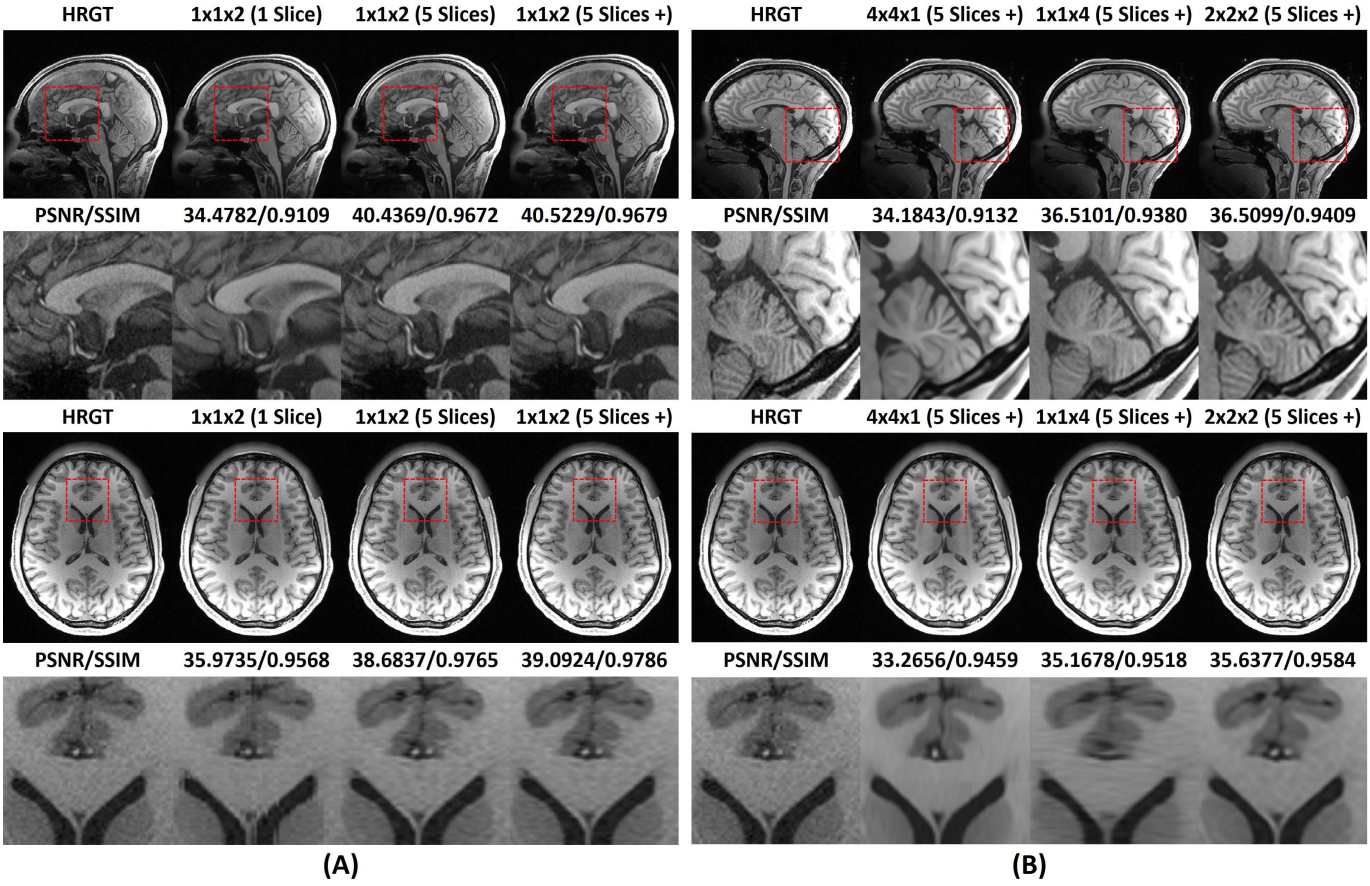

Fig. 5: Qualitative comparison of super resolution. Left: SR in single-slice and thin-slab mode; Right: different down-sampling strategies with acceleration factor of 4.

TABLE II: Comparison with the MRI super resolution state-of-the-art methods (red represents the best and blue represents the second best)

Model	Scale Factor	# Ops (GFlops)	GPU Consumption (GB)	Inference Time (s)	Axial SSIM / PSNR	Sagittal SSIM / PSNR	Coronal SSIM / PSNR
3D SRCNN (1)	2 × 2 × 1	13.841	2.48	3.00	0.9553±0.0060 / 37.4862±1.7117	0.9540±0.0062 / 36.8319±1.7755	0.9550±0.0059 / 36.8086±2.0677
3D FSRCNN (2)		7.079	3.22	3.68	0.9553±0.0061 / 37.5287±1.7527	0.9540±0.0062 / 36.8748±1.8162	0.9550±0.0060 / 36.8593±2.1108
DCSRN (10)		57.50	9.35	10.84	0.9548±0.0061 / 37.4481±1.7021	0.9535±0.0063 / 36.8042±1.7672	0.9545±0.0060 / 36.7795±2.0488
mDCSRN (11)		107.54	14.13	28.16	0.9604±0.0051 / 38.2239±1.5180	0.9591±0.0053 / 37.5905±1.5706	0.9602±0.0050 / 37.6437±1.8080
ReCNN (36)		522.74	3.74	26.48	0.9603±0.0070 / 37.9635±1.9943	0.9591±0.0070 / 37.2667±2.1139	0.9601±0.0069 / 37.3639±2.3610
MINet (37)		79.05	3.83	38.74	0.9635±0.0051 / 39.2734±1.4081	0.9625±0.0053 / 38.7541±1.4350	0.9633±0.0051 / 38.7810±1.6106
TS-RCAN (Ours)		9.12	1.48	5.93	0.9638±0.0049 / 39.3688±1.3533	0.9631±0.0051 / 38.8662±1.3566	0.9637±0.0049 / 38.9178±1.5334
TS-RCAN+ (Ours)		9.12	1.48	5.93	0.9644±0.0049 / 39.4410±1.3675	0.9634±0.0051 / 38.9355±1.3756	0.9643±0.0049 / 38.9922±1.5492
3D SRCNN (1)	4 × 4 × 1	13.841	2.48	3.02	0.9060±0.0096 / 33.9566±1.1739	0.8995±0.0105 / 33.1843±1.2890	0.9053±0.0096 / 33.0890±1.4631
3D FSRCNN (2)		7.079	3.22	3.68	0.9052±0.0088 / 33.8116±1.1595	0.8984±0.0095 / 33.0282±1.2994	0.9043±0.0089 / 32.9588±1.4213
DCSRN (10)		57.50	9.35	10.83	0.9050±0.0096 / 33.8680±1.1419	0.8984±0.0105 / 33.1024±1.2735	0.9042±0.0095 / 33.0070±1.4217
mDCSRN (11)		107.54	14.13	28.13	0.9209±0.0099 / 34.9411±1.3289	0.9159±0.0108 / 34.1952±1.4493	0.9205±0.0098 / 34.1947±1.5905
ReCNN (36)		522.74	3.74	26.50	0.9260±0.0116 / 35.1404±1.5382	0.9219±0.0119 / 34.3217±1.7724	0.9257±0.0115 / 34.4447±1.9166
MINet (37)		91.3	3.83	43.86	0.9376±0.0091 / 36.4424±1.4764	0.9345±0.0096 / 35.8028±1.5047	0.9375±0.0090 / 35.8137±1.5086
TS-RCAN (Ours)		7.40	1.62	7.17	0.9320±0.0098 / 36.2141±1.5265	0.9291±0.0098 / 35.6303±1.4204	0.9318±0.0096 / 35.6557±1.5058
TS-RCAN+ (Ours)		7.40	1.62	7.17	0.9347±0.0097 / 36.4120±1.5599	0.9300±0.0100 / 35.7243±1.4502	0.9345±0.0096 / 35.8613±1.5470
3D SRCNN (1)	2 × 2 × 2	13.841	2.48	3.03	0.9420±0.0080 / 36.6352±1.5233	0.9403±0.0081 / 35.8376±1.6609	0.9418±0.0077 / 35.9467±1.8111
3D FSRCNN (2)		7.079	3.22	3.71	0.9422±0.0074 / 36.6646±1.5445	0.9405±0.0075 / 35.8810±1.6745	0.9420±0.0071 / 35.9862±1.8328
DCSRN (10)		57.50	9.35	10.79	0.9415±0.0074 / 36.6051±1.5247	0.9398±0.0075 / 35.8276±1.6557	0.9413±0.0072 / 35.9221±1.8079
mDCSRN (11)		107.54	14.13	28.12	0.9486±0.0069 / 37.1047±1.4981	0.9469±0.0071 / 36.3776±1.6359	0.9484±0.0067 / 36.4723±1.7629
ReCNN (36)		522.74	3.74	26.47	0.9499±0.0077 / 37.2740±1.7676	0.9483±0.0077 / 36.4986±1.9425	0.9498±0.0075 / 36.6909±2.1169
MINet (37)		79.14	4.05	18.86	0.9512±0.0090 / 38.1000±1.6055	0.9499±0.0092 / 37.5841±1.6987	0.9512±0.0089 / 37.6675±1.5216
TS-RCAN (Ours)		9.19	1.48	2.97	0.9501±0.0078 / 38.1622±1.3875	0.9491±0.0079 / 37.5689±1.3742	0.9499±0.0078 / 37.6385±1.3457
TS-RCAN+ (Ours)		9.19	1.48	2.97	0.9514±0.0078 / 38.3026±1.4161	0.9498±0.0080 / 37.7166±1.4138	0.9513±0.0077 / 37.7945±1.3834

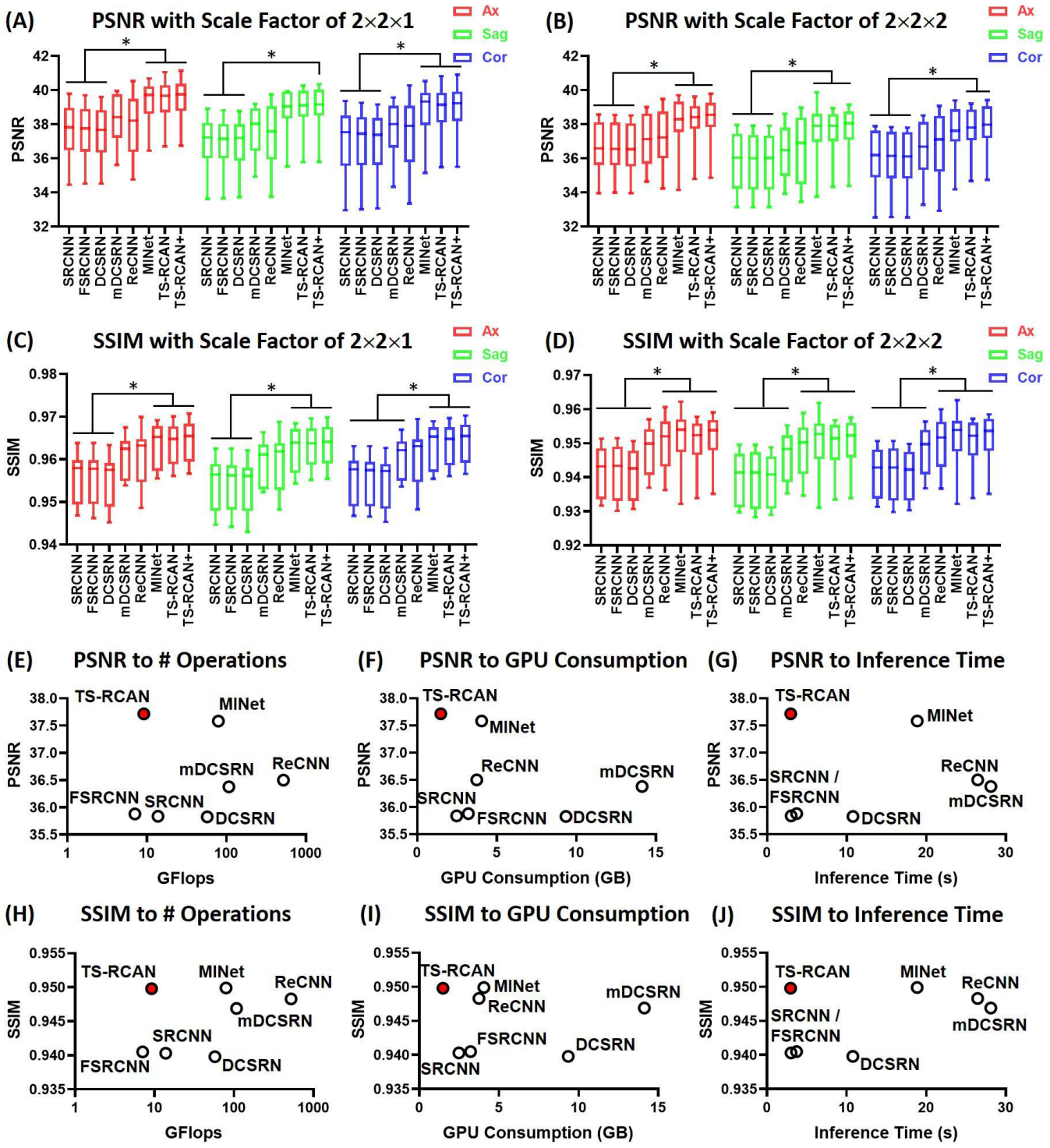

Fig. 6: Comparison of our network with other state-of-the-art 3D networks. (A)-(D): comparison of metrics with two scale factors ($2 \times 2 \times 1$ and $2 \times 2 \times 2$), '+' represents the SR reconstruction with self-ensemble. Mann-Whitney U tests compared whether the metrics of different down-sampling strategies were statistically different. Significant difference is indicated with $*p < 0.05$ and $**p < 0.0005$. (E)-(J): Comparison of number of operations, GPU consumption and inference time to PSNR and SSIM with scale factor of $2 \times 2 \times 2$.

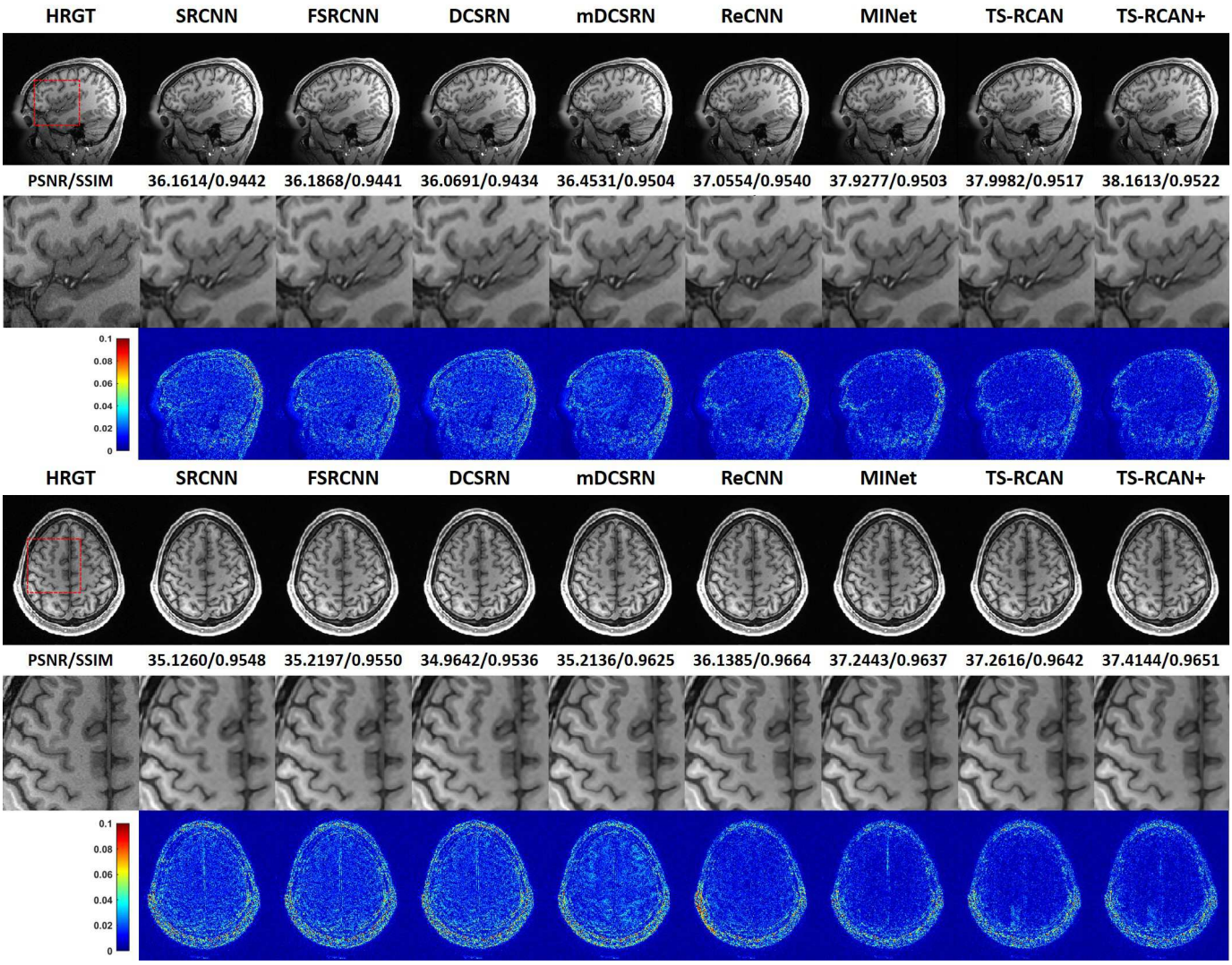

Fig. 7: Qualitative comparison with the MRI super resolution state-of-the methods with down-sampling factor of $2 \times 2 \times 2$.

Fig.9 depicts an example of images in the axial and sagittal planes with motion artifacts reduced from the worst case. On the axial plane, the UNet corrected image contains several incorrectly restored anatomical structures when compared to the ground truth, whereas with our network in 2D mode, the quality of the restored image is improved with minor anatomical structure errors. And in 3D mode, our model provides significantly improved image quality, with the majority of features retained and very well represented. The difference between the models is even greater in the sagittal plane. Due to a lack of through-slice information, the UNet generated image contains a severe through-slice mismatch, which is slightly reduced by our model in 2D mode and significantly reduced in 3D mode.

D. Restoration with Uncertainty

The uncertainty maps were generated simultaneously with the restored images using our network with NIG loss. In this section, the aleatoric and epistemic uncertainty for the super resolution task will be qualitatively and quantitatively evaluated. Firstly, an example of an HRGT image with the corresponding SR image, absolute error map, uncertainty maps, and SSIM map are shown in Fig.10. As mentioned in the method section, out-of-distribution data can be identified with epistemic uncertainty but not with aleatoric uncertainty alone [31]. As shwon in Fig.10(D), the aleatoric uncertainty pervades over the whole image volume, including the background region, whereas the epistemic uncertainty map in Fig.10(E) shows significantly emphasized regions in specific anatomical structures. Furthermore, the regions with high values in the epistemic uncertainty map correspond to the regions with higher error in the absolute error map (Fig.10(F)) and lower SSIM in the SSIM map (Fig.10(C)), and vice versa.

In addition, by investigating the relationships between the mean epistemic uncertainty of each image slice and their SSIM/PSNR values and observed strong correlations between them. As shown in Fig.10(G)(H), we first performed linear regression on the pairs of mean epistemic and SSIM values using the 10 datasets from the test group (blue dots), and obtained a linear regression (the red solid line) with a 95% prediction interval (the region between the red dashed lines).

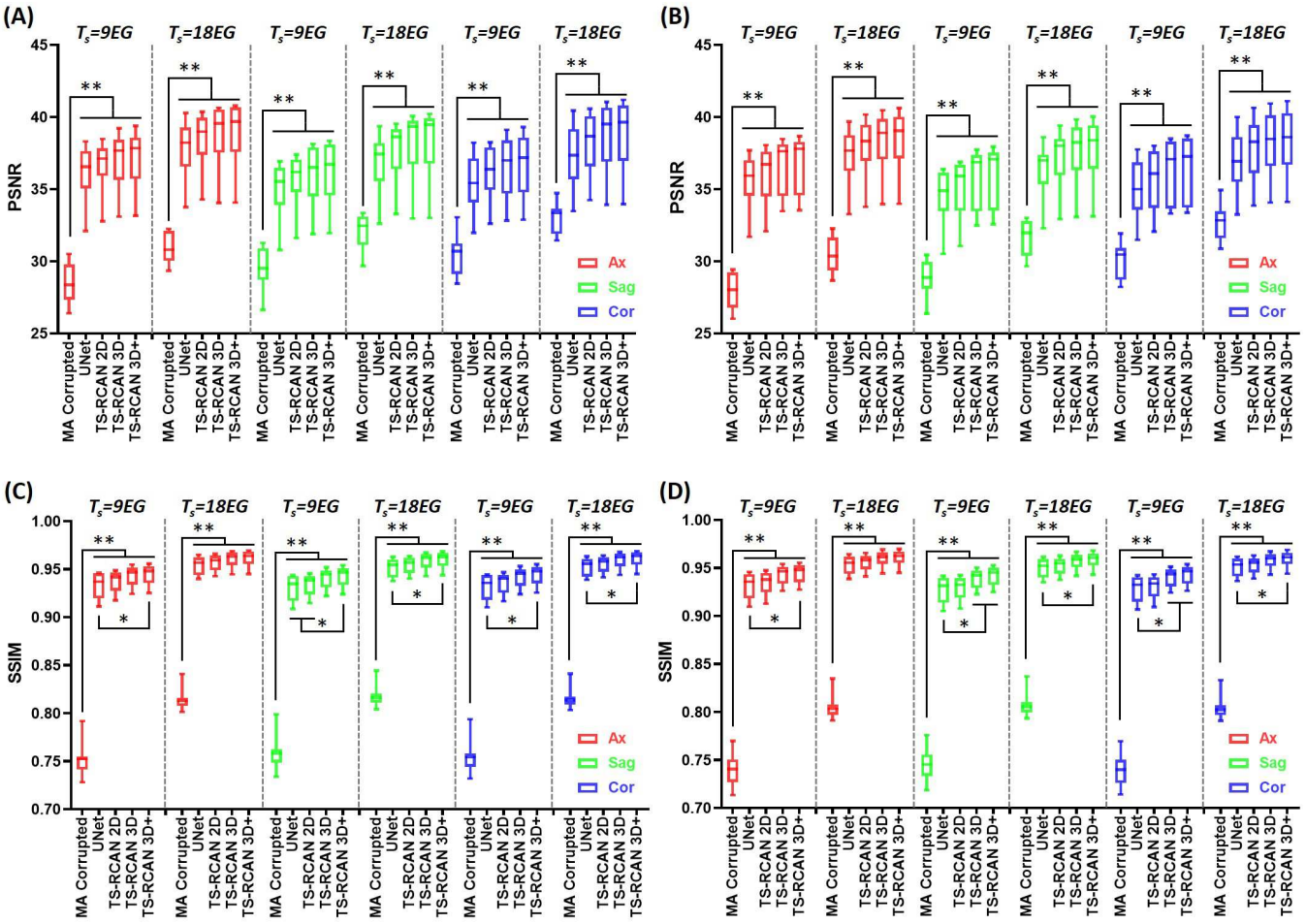

Fig. 8: Comparison of PSNR and SSIM of images with motion-artifact and corrected by UNet and TS-RCAN. (A) and (C): with 5° in-plane rotation and 0° through-plane rotation. (B) and (D): with 5° in-plane rotation and 5° through-plane rotation. '+' represents the SR reconstruction with self-ensemble. Mann-Whitney U tests compared whether the metrics of different networks were statistically different. Significant difference is indicated with $*p < 0.05$ and $**p < 0.0005$.

Due to the logarithmic function of PSNR, an exponential regression was performed on the pairs of mean epistemic and PSNR values, and a regression equation with a 95% prediction interval was also obtained. The R^2 values of the regressions were greater than 0.8, indicating that the regressions fit the data well. Then, we included 40 additional datasets, which were isolated from the training/validation/test groups, to validate the accuracy of the regressions in predicting the SSIM and PSNR from the mean epistemic uncertainty values. The additional 40 datasets are represented as green crosses in Fig.10(G)(H) with approximately 95% of the data located in the prediction intervals for all regressions, indicating that the correlations between mean epistemic uncertainty and SSIM/PSNR closely follow the predicted distribution. Therefore, the proposed method can predict the SSIM and PSNR values when ground truth is not available in clinical settings.

IV. Conclusion

In this manuscript, we first proposed a method using the TS-RCAN network for the restoration of 3D high-quality MR images. In the SR task, our network outperformed 3D networks in all down-sampling strategies, while consuming down to 39.6%/36.5% of GPU resources and less than 11.2%/15.7% of inference time compared to ReCNN/MINet, indicating that it can be easily deployed on any consumer GPU. In the MAR task, our network in 2D mode performed significantly better than the UNet, and it further improved its performance in 3D mode by enhancing through-slice agreement. Besides, our method can be extended by using a 3D network to process 4D images, for instance, enhancing temporal and spatial resolutions simultaneously.

In addition, we compared various combinations of in-plane and through-plane down-sampling with different scale factors. Our experiments revealed that using $1 \times 1 \times 2$ for $\times 2$ acceleration and $2 \times 2 \times 2$ for $\times 4$ acceleration results in the best SR reconstruction performance. Therefore, these down-sampling strategies are recommended for acquiring real LR images when applying deep learning-based SR reconstruction in clinical environment.

Furthermore, we proposed a novel method for retrospective motion artifact generation. A predefined motion pattern with

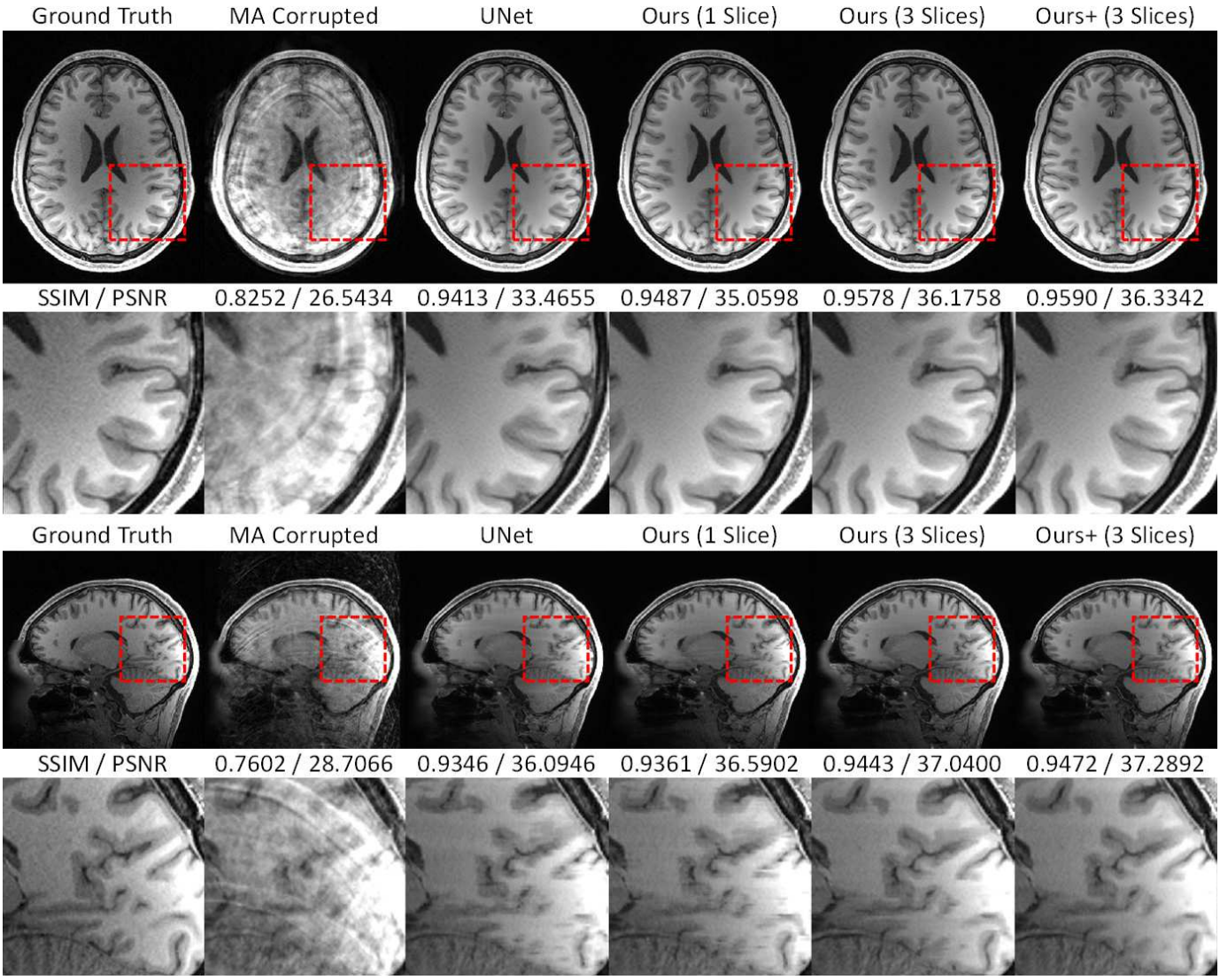

Fig. 9: Comparison of visual effect on axial and sagittal planes among methods for MAR with $T_S = 9EG$ and the combination of 5 degrees in-plane and through-plane rotation.

adjustable duration and frequency of movement was used in our method, resulting in controllable and quantifiable severity of the generated motion artifacts. Motion artifacts corrupted images with linearly increased SSIM and PSNR values were obtained by varying the frequency of movement in our experiments. The motion pattern can be adjusted based on any specific scenario.

Finally, we used evidential regression learning to generate uncertainty maps using our network simultaneously with the reconstructed images. The generated epistemic uncertainty map corresponded to the absolute error and SSIM map between the ground truth and the reconstructed image. In addition, we investigated the relationship between epistemic uncertainty and the SSIM/PSNR values. Our experiments revealed that the mean uncertainty of each image slice was linearly and exponentially related to the SSIM and PSNR, respectively. Therefore, when ground truth is not available in clinical settings, the SSIM and PSNR values can be predicted using the regression equations derived from pairs of images from the test dataset.

REFERENCES

[1] Dong, C., Loy, C.C., He, K., Tang, X., 2016. Image super-resolution using deep convolutional networks. IEEE transactions on pattern analysis and machine intelligence 38, 295-307.

[2] Dong, C., Loy, C.C., Tang, X., 2016. Accelerating the super-resolution convolutional neural network, in: European Conference on Computer Vision, Springer. pp. 391-407.

[3] Sun, S., Chen, W., Wang, L., Liu, X., Liu, T.Y., 2016. On the depth of deep neural networks: A theoretical view., in: AAAI, pp. 2066-2072.

[4] Glorot, X., Bengio, Y.. Understanding the difficulty of training deep feedforward neural networks, in: Proceedings of the Thirteenth International Conference on Artificial Intelligence and Statistics 2010, 249-256.

[5] Kaiming He, Xiangyu Zhang, Shaoqing Ren, Jian Sun: Deep Residual Learning for Image Recognition. IEEE Conference on Computer Vision and Pattern Recognition (CVPR), 2016.

[6] Yulun Zhang, Kunpeng Li, Kai Li, Lichen Wang, Bineng Zhong, Yun Fu; Proceedings of the European Conference on Computer Vision (ECCV), 2018, pp. 286-301.

[7] Lin, Z., Garg, P., Banerjee, A., Magid, S. A., Sun, D., Zhang, Y., Gool, L. V., Wei, D., Pfister, H. (2022). Revisiting RCAN: Improved training for image super-resolution. arXiv preprint arXiv:2201.11279.

[8] Litjens, G., Kooi, T., Bejnordi, B.E., Setio, A.A.A., Ciompi, F., Ghafoorian, M., van der Laak, J.A., van Ginneken, B., Sanchez, C.I.. A survey on deep learning in medical image analysis. Medical image analysis 2017 42, 60-88.

[9] Oktay, O., Bai, W., Lee, M., Guerrero, R., Kamnitsas, K., Caballero, J., de Marvao, A., Cook, S., ORegan, D., Rueckert, D., 2016. Multi-input cardiac image super-resolution using convolutional neural networks, in: International Conference on Medical Image Computing and Computer-Assisted Intervention, Springer. pp. 246-254.

[10] You, C., Li, G., Zhang, Y., Zhang, X., Shan, H., Li, M., Ju, S., Zhao, Z., Zhang, Z., Cong, W., et al., 2019. CT super-resolution GAN constrained by the identical, residual, and cycle learning ensemble (GAN-CIRCLE). IEEE Transactions on Medical Imaging 39, 188-203.

[11] Wang, S., Su, Z., Ying, L., Peng, X., Zhu, S., Liang, F., Feng, D., Liang, D., 2016. Accelerating magnetic resonance imaging via deep learning, in: Biomedical Imaging (ISBI), 2016 IEEE 13th International Symposium on, IEEE. pp. 514-517.

[12] Chen, Y et al.. Brain MRI Super Resolution Using 3D Deep Densely Connected Neural Networks. 2018 IEEE 15th International Symposium on Biomedical Imaging.

[13] Chen, Y et al.. Efficient and Accurate MRI Super-Resolution using a Generative Adversarial Network and 3D Multi-Level Densely Connected Network, 2018 MICCAI, pp. 91– 99.

[14] Pham, C.H., Ducournau, A., Fablet, R., Rousseau, F., 2017. Brain MRI super resolution using deep 3D convolutional networks, in: Biomedical Imaging (ISBI 2017), 2017 IEEE 14th International Symposium on, IEEE. pp. 197-200.

[15] Xiaole Zhao, Yulun Zhang, Tao Zhang, and Xueming Zou. Channel Splitting Network for Single MR Image Super-Resolution. IEEE TRANSACTIONS ON IMAGE PROCESSING 2019, 28, 5649-5662.

[16] Pham C H, Tor-Díez C, Meunier H, et al. Multiscale brain MRI super-resolution using deep 3D convolutional networks. Computerized Medical Imaging and Graphics, 2019, 77: 101647.

[17] Evan M. Masutani, Naeim Bahrami, Albert Hsiao. Deep Learning Single-Frame and Multiframe Super-Resolution for Cardiac MRI. Radiology 2020; 295:

[18] Akshay S. Chaudhari, Zhongnan Fang, Feliks Kogan, Jeff Wood, Kathryn J. Stevens, Eric K. Gibbons, Jin Hyung Lee, Garry E. Gold, Brian A. Hargreaves. Super-resolution musculoskeletal MRI using deep learning. Magn Reson Med 2018; 80: 2139-2154.

[19] ZHANG SIYUAN, DONG JINGXIAN, JIANG CAIWEN, HOU WENGUANG, DENG XIANBO. 2D CNN-Based Slices-to-Volume Superresolution Reconstruction. IEEE Access 2020, 8, 86357-86366.

[20] Wei Lu, Zhijin Song, Jinghui Chu. A novel 3D medical image super-resolution method based on densely connected network. Biomedical Signal Processing and Control 2020, 62, 102120.

[21] Küstner T, Armanious K, Yang J, Yang B, Schick F, Gatidis S. Retrospective Correction of Motion-affected MR Images using Deep Learning Frameworks. Magn Reson Med 2019; 82: 1527-1540.

[22] Johnson PM, Drangova M. Conditional generative adversarial network for 3D rigid-body motion correction in MRI. Magn Reson Med 2019; 82: 901-910.

[23] Chunga, H et al.. Simultaneous super-resolution and motion artifact removal in diffusion-weighted MRIusing unsupervised deep learning. arXiv:2105.00240v1

[24] Chengyan Wanga, Yucheng Liang, Yuan Wu, Siwei Zhao, Yiping P. Du. Correction of out-of-FOV motion artifacts using convolutional neural network. Magnetic Resonance Imaging 2020, 71, 93-102.

[25] Ben A Duffy, Lu Zhao, Farshid Sepehrband, Joyce Min, DannyJJ Wang, Yonggang Shi, Arthur W Toga, Hosung Kim. Retrospective motion artifact correction of structural MR images using deep learning improves the quality of cortical surface reconstructions. NeuroImage 230 (2021) 117756.

[26] Gyutaek Oh, Jeong Eun Lee, and Jong Chul Ye. Unpaired MR Motion Artifact Deep Learning Using Outlier-Rejecting Bootstrap Aggregation. IEEE TMI.2021.3089708.

[27] Seul Lee, Soozy Jung, Kyu-Jin Jung, Dong-Hyun Kim. Deep Learning in MR Motion Correction: a Brief Review and a New Motion Simulation Tool (view2Dmotion). iMRI 2020;24:196-206.

[28] Ryutaro Tanno, Daniel E. Worrall, Enrico Kaden, Aurobrata Ghosh, Francesco Grussu, Alberto Bizzi, Stamatios N. Sotiropoulos, Antonio Criminisi, Daniel C. Alexander. Uncertainty Quantification in Deep Learning for Safer Neuroimage Enhancement. arXiv:1907.13418v1.

[29] Yu Qin, Zhiwen Liu, Chenghao Liu, Yuxing Li, Xiangzhu Zeng, Chuyang Ye. Super-Resolved q -Space deep learning with uncertainty quantification. Medical Image Analysis 2021; 67: 101885.

[30] Balaji Lakshminarayanan, Alexander Pritzel, Charles Blundell. Simple and Scalable Predictive Uncertainty Estimation using Deep Ensembles. NIPS 2017.

[31] Alex Kendall, Yarin Gal. What Uncertainties Do We Need in Bayesian Deep Learning for Computer Vision? NIPS 2017.

[32] Allen-Zhu Z, Li Y. Towards understanding ensemble, knowledge distillation and self-distillation in deep learning. arXiv preprint arXiv:2012.09816, 2020.

[33] Feng R, Gu J, Qiao Y, et al. Suppressing model overfitting for image super-resolution networks. Proceedings of the IEEE/CVF Conference on Computer Vision and Pattern Recognition Workshops. 2019: 0-0.

[34] Alexander Amini, Wilko Schwarting, Ava Soleimany, Daniela Rus. Deep Evidential Regression. NeurIPS 2020.

[35] Hang Zhao, Orazio Gallo, Iuri Frosio, and Jan Kautz: Loss Functions for Image Restoration With Neural Networks. IEEE Transactions on Computational Imaging, 2017.

[36] Barron JT, A General and Adaptive Robust Loss Function. arXiv:1701.03077.

[37] Zhou Wang, Alan C. Bovik, Hamid R. Sheikh, Eero P. Simoncelli: Image Quality Assessment: From Error Visibility to Structural Similarity. IEEE Transactions on Image Processing, 2004.

[38] Evan M. Masutani, Naeim Bahrami, Albert Hsiao. Deep Learning Single-Frame and Multiframe Super-Resolution for Cardiac MRI. Radiology 2020; 295:

[39] Van Essen, D.C., Smith, S.M., Barch, D.M., Behrens, T.E., Yacoub, E., Ugurbil, K., Consortium, W.M.H., et al., 2013. The WU-Minn human connectome project: an overview. Neuroimage 80, 62-79.

[40] Kim J, Lee J K, Lee K M. Accurate image super-resolution using very deep convolutional networks. Proceedings of the IEEE conference on computer vision and pattern recognition. 2016: 1646-1654.

[41] Tai Y, Yang J, Liu X. Image super-resolution via deep recursive residual network. Proceedings of the IEEE conference on computer vision and pattern recognition. 2017: 3147-3155.

[42] Dong C, Loy C C, He K, et al. Image super-resolution using deep convolutional networks. IEEE transactions on pattern analysis and machine intelligence, 2015, 38(2): 295-307.

[43] C. Dong, C. C. Loy, and X. Tang, “Accelerating the super-resolution convolutional neural network,” in Proc. Eur. Conf. Comput. Vis., 2016, pp. 391–407

[44] Feng C M, Fu H, Yuan S, et al. Multi-contrast mri super-resolution via a multi-stage integration network. International Conference on Medical Image Computing and Computer-Assisted Intervention. Springer, Cham, 2021: 140-149.

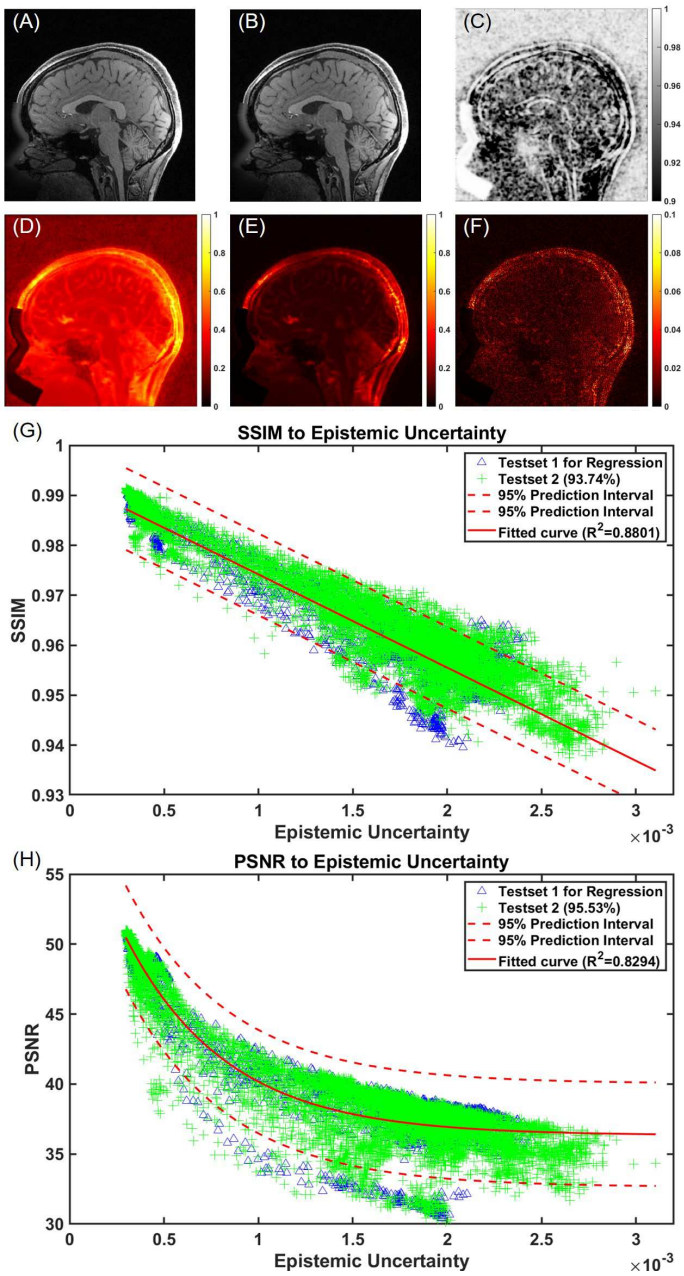

Fig. 10: Visual effect of aleatoric and epistemic uncertainty: (A): high-resolution ground truth (HRGT) image; (B): super-resolution (SR) image; (C): SSIM map; (D): aleatoric uncertainty map; (E): epistemic uncertainty map; (F): absolute error between HRGT and SR images; (G)/(H): Regression of SSIN/PSNR to epistemic uncertainty.

TABLE III: Motion Artifact Reduction Performance (red represents the best and blue represents the second best)

Degrees of Rotation	T_s	Direction	MA Corrupted SSIM / PSNR	UNet (20) SSIM / PSNR	TS-RCAN 2D SSIM / PSNR	TS-RCAN 3D SSIM / PSNR	TS-RCAN 3D+ SSIM / PSNR
In-plane :5° Through-plane: 0°	9EG	Axial	0.7515±0.0169 28.4205±1.3214	0.9334±0.0131 36.1477±1.9409	0.9378±0.0105 36.6720±1.7549	0.9434±0.0100 37.0669±1.9089	0.9447±0.0100 37.1948±1.9539
		Sagittal	0.7584±0.0170 29.4601±1.4077	0.9308±0.0130 34.9310±1.9327	0.9346±0.0105 35.6838±1.8346	0.9407±0.0100 36.1504±2.0565	0.9431±0.0100 36.2989±2.1084
		Coronal	0.7540±0.0167 30.4709±1.3599	0.9318±0.0128 35.4887±1.9717	0.9359±0.0103 36.2080±1.8509	0.9421±0.0097 36.6596±2.0911	0.9443±0.0098 36.8058±2.1399
	18EG	Axial	0.8142±0.0107 30.9466±1.1017	0.9547±0.0092 37.8081±1.9280	0.9573±0.0083 38.4131±1.9999	0.9608±0.0081 38.7964±2.1929	0.9615±0.0082 38.8977±2.2360
		Sagittal	0.8176±0.0109 32.1021±1.2554	0.9524±0.0092 36.8721±1.9940	0.9550±0.0084 37.6460±2.1414	0.9588±0.0082 38.1481±2.3806	0.9601±0.0082 38.2692±2.4290
		Coronal	0.8151±0.0104 33.0248±1.0399	0.9533±0.0090 37.3270±2.1011	0.9560±0.0082 38.1568±2.1603	0.9599±0.0080 38.6287±2.3530	0.9611±0.0081 38.7481±2.4005
	36EG	Axial	0.8843±0.0104 34.6632±0.8334	0.9726±0.0068 40.2495±2.3249	0.9742±0.0063 41.0761±2.4175	0.9762±0.0059 41.3078±2.4350	0.9766±0.0059 41.3979±2.4630
		Sagittal	0.8853±0.0107 35.9299±1.1522	0.9711±0.0069 39.6977±2.4025	0.9728±0.0064 40.6618±2.7105	0.9749±0.0060 40.9495±2.7473	0.9756±0.0060 41.0564±2.7804
		Coronal	0.8840±0.0105 36.7171±0.7657	0.9718±0.0068 40.1851±2.4817	0.9734±0.0063 41.1209±2.6501	0.9756±0.0059 41.4039±2.6381	0.9762±0.0059 41.5084±2.6706
	72EG	Axial	0.9335±0.0088 37.9792±0.8041	0.9815±0.0039 42.4534±1.3211	0.9824±0.0034 43.0007±1.6444	0.9838±0.0031 43.3416±1.7077	0.9841±0.0031 43.4338±1.7216
		Sagittal	0.9330±0.0090 39.0887±1.0497	0.9804±0.0040 42.2210±1.3611	0.9813±0.0036 42.8613±1.8812	0.9829±0.0033 43.2812±2.0039	0.9833±0.0032 43.3887±2.0212
		Coronal	0.9331±0.0089 39.7543±0.8666	0.9810±0.0039 42.7195±1.4563	0.9819±0.0035 43.2997±1.8700	0.9834±0.0032 43.6940±1.9586	0.9838±0.0031 43.8021±1.9774
In-plane :5° Through-plane: 5°	9EG	Axial	0.7391±0.0164 27.8964±1.2784	0.9319±0.0135 35.5853±1.9099	0.9349±0.0118 36.0326±1.9881	0.9428±0.0100 36.6468±1.9395	0.9442±0.0100 36.7868±1.9976
		Sagittal	0.7448±0.0164 28.8895±1.2416	0.9277±0.0135 34.4722±1.9215	0.9296±0.0118 35.0965±2.0324	0.9390±0.0100 35.8074±2.0464	0.9417±0.0100 35.9679±2.1138
		Coronal	0.7393±0.0163 30.0419±1.2217	0.9285±0.0132 35.0814±2.0618	0.9308±0.0116 35.7180±2.1098	0.9402±0.0098 36.3734±2.1403	0.9428±0.0098 36.5292±2.2031
	18EG	Axial	0.8051±0.0126 30.4936±1.2426	0.9538±0.0091 37.3098±1.8428	0.9564±0.0081 37.9584±1.9416	0.9601±0.0078 38.3078±2.0456	0.9609±0.0078 38.4133±2.0892
		Sagittal	0.8072±0.0127 31.6580±1.3244	0.9506±0.0093 36.4039±1.8100	0.9529±0.0084 37.1884±1.9752	0.9574±0.0079 37.6302±2.1192	0.9590±0.0079 37.7503±2.1663
		Coronal	0.8042±0.0123 32.7122±1.1905	0.9514±0.0090 36.9730±1.9727	0.9539±0.0081 37.7629±2.0756	0.9584±0.0077 38.1980±2.1605	0.9598±0.0078 38.3160±2.2087
	36EG	Axial	0.8798±0.0101 34.2659±0.8973	0.9726±0.0064 40.0343±1.9182	0.9742±0.0065 40.6765±2.2403	0.9760±0.0068 41.0267±2.5286	0.9764±0.0068 41.1266±2.5569
		Sagittal	0.8801±0.0105 35.5330±1.2195	0.9708±0.0066 39.4258±1.9870	0.9721±0.0067 40.2061±2.4793	0.9744±0.0069 40.7339±2.7964	0.9751±0.0069 40.8523±2.8276
		Coronal	0.8786±0.0103 36.4028±0.7436	0.9713±0.0064 40.0170±2.0476	0.9728±0.0066 40.7534±2.4718	0.9750±0.0069 41.2443±2.7708	0.9757±0.0069 41.3611±2.8007
	72EG	Axial	0.9301±0.0086 37.5567±0.8004	0.9804±0.0039 41.5370±1.4301	0.9815±0.0035 42.1384±1.7698	0.9830±0.0032 42.4736±1.7286	0.9834±0.0031 42.5703±1.7533
		Sagittal	0.9291±0.0090 38.6985±1.0089	0.9789±0.0041 41.1460±1.6552	0.9799±0.0038 41.8921±2.2112	0.9818±0.0033 42.2759±2.2483	0.9823±0.0033 42.3826±2.2796
		Coronal	0.9290±0.0088 39.4717±1.0261	0.9795±0.0040 41.7945±1.5527	0.9805±0.0036 42.4655±1.9961	0.9823±0.0032 42.8263±1.9975	0.9828±0.0032 42.9356±2.0272